ACS Catalysis

Research Article

pubs.acs.org/acscatalysis

Platinum and Palladium Overlayers Dramatically Enhance the Activity of Ruthenium Nanotubes for Alkaline Hydrogen Oxidation

Samuel St. John,[†] Robert W. Atkinson, III,[†] Kinga A. Unocic,[‡] Raymond R. Unocic,[§] Thomas A. Zawodzinski, Jr.,[†,‡] and Alexander B. Papandrew*,[†]

[†]Chemical and Biomolecular Engineering, University of Tennessee, Knoxville, Tennessee, United States

[‡]Materials Science and Technology Division, Oak Ridge National Laboratory, Oak Ridge, Tennessee, United States

[§]Center for Nanophase Materials Sciences, Oak Ridge National Laboratory, Oak Ridge, Tennessee, United States

Supporting Information

ABSTRACT: Templated vapor synthesis and thermal annealing were used to synthesize unsupported metallic Ru nanotubes with Pt or Pd overlayers. By controlling the elemental composition and thickness of these overlayers, we obtain nanostructures with very high alkaline hydrogen oxidation activity. Nanotubes with a nominal atomic composition of $Ru_{0.90}Pt_{0.10}$ display a surface-specific activity (2.4 mA/cm^2) that is 35 times greater than that of pure Ru nanotubes at a 50 mV overpotential and ~2.5 times greater than that of pure Pt nanotubes (0.98 mA/cm^2). The surface-segregated structure also confers dramatically increased Pt utilization efficiency. We find a platinum-mass-specific activity of 1240 A/g_{Pt} for the optimized nanotube versus 280 A/g_{Pt} for carbon-supported Pt nanoparticles and 109 A/g_{Pt} for monometallic Pt nanotubes. We attribute the enhancement of both area- and platinum-mass-specific activity to the atomic-scale homeomorphism of the nanotube form factor with adlayer-modified polycrystals. In this case, subsurface ligand and bifunctional effects previously observed on segregated, adlayer-modified polycrystals are translated to nanoscale catalysts.

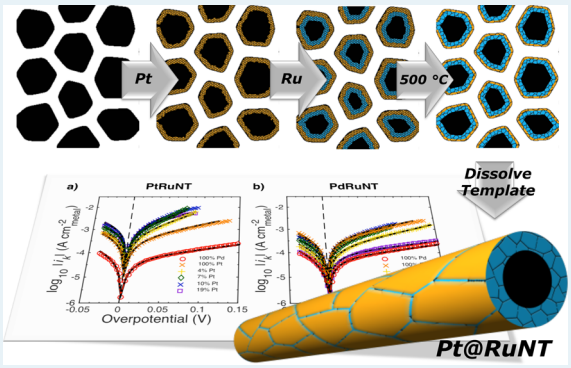

KEYWORDS: *alkaline anode, electrocatalysts, ruthenium-rich, nanoparticle alloy, fuel cell, chemical vapor deposition*

INTRODUCTION

With recent advances in stable and conductive alkaline anion exchange membranes (AAEMs),[1,2] alkaline anion exchange membrane fuel cells (AAEMFCs) have emerged as an alternative technology to proton exchange membrane fuel cells (PEMFCs). The relatively less-corrosive environment of AAEMFCs allow for inexpensive oxygen reduction reaction (ORR) electrocatalysts, such as silver,[3] without the concern of membrane fouling from catalyst dissolution during operation. However, this advantage is obviated by the slow hydrogen oxidation reaction (HOR) kinetics at the anode, where gains at the cathode are offset by a 100-fold reduction in anodic exchange current density.[4] The creation of suitable HOR catalysts for alkaline pH is now required to fulfill the promise of AAEMFCs.

Two different hypotheses have been proposed in the literature to describe routes to improved HOR activity and paths toward more-active catalysts. The first details a bifunctional route, whereby promoting hydroxyl adsorption onto the electrocatalyst surface enhances HOR activity by clearing active sites for slow dissociative hydrogen adsorption.[5] Alternatively, it has been proposed that an electronic modification of the electrocatalyst surface to reduce hydrogen-binding energy accelerates the HOR.[6−8] We previously addressed the observed enhancement in the electrocatalytic HOR activity of Ru_xPt_y and Ru_xPd_y alloy nanoparticles (NPs) in rotating-disk electrode measurements in 0.1 M KOH.[4] As the binding energy of hydrogen was reduced, hydrogen dissociative adsorption (Tafel step) emerged as being rate-limiting on Pt−Ru nanoparticles.[9] However, in the case of Pd−Ru, the hydrogen binding energy was not sufficiently reduced to observe the emergence of H_2 dissociative adsorption as being rate-limiting. In this way, we have observed both ligand and bifunctional effects in the alloy nanoparticles via the characteristic differences in the electrochemical kinetic data.

Our results in the case of supported NP catalysts motivated us to investigate systems with greater structural clarity to probe the effects of the Pt and Pd additions to Ru. Foundational work has been performed for decades using bulk-like polycrystals,[10−15] and recent studies have shown that adlayers can modify the properties of the combined materials significantly, in comparison with the bulk. Examples include monometallic and mixed monolayers of Pt on Ru,[16−20] Pd,[21,22] and Ni,[23] as well as Bi on Pt[24] and Co on Pt.[25,26] Importantly, the adlayers must be

Received: July 9, 2015
Revised: September 16, 2015

 © XXXX American Chemical Society

DOI: 10.1021/acscatal.5b01432
ACS Catal. 2015, 5, 7015−7023

of optimal thickness and coverage to generate active, metallic Pt without sacrificing the electronic effects from the subsurface element or support on the outermost atomic layer.[27−29] When appropriately designed, such systems can display enhanced activity through ligand effects while retaining the stability of the bulk polycrystals. Ligand effects have been enhanced further for select electrochemical reactions when the proximal distribution of bifunctional active sites is carefully controlled via submonolayer coverage. A classic example is found in enhanced ethanol oxidation by co-locating oxophilic atoms, such as Sn, near Pt active sites.[30−32]

Segregated Pt atop Ru has been used to optimize the binding of reactive intermediates for improved oxygen reduction[33,34] and CO-tolerant H_2 oxidation[35] in proton exchange membrane fuel cells. For oxygen reduction, moderate binding properties were produced such that both hydrogenation of O/OH and O−O scission were active. When applied to CO-tolerant H_2 oxidation, optimized ligand effects and Pt surface layer compression of ∼0.6%−1.0% lead to reduced CO binding energy and improved tolerance to poisoning.

A recurring challenge has been translating these effects into comparably active high-surface-area catalysts. We thus consider the case of so-called extended surface catalysts, which bridge the gap between polycrystals and nanoparticles. These are essentially hybrid materials, retaining the high surface-specific activity and stability of the bulk while attaining the high surface areas of nanostructured practical catalysts.

Techniques for generating thin overlayers (or shells) include galvanic displacement,[36,37] chemical processing,[38,39] or ligand-mediated solution phase synthesis.[40−43] We have developed a synthesis approach based on vapor deposition from metal-organic precursors on functional supports or monolithic sacrificial templates. This approach can be used to fabricate multicomponent highly dispersed or conformal coatings on arbitrary supports simply and effectively.[44−48] Subsequent heat treatments and/or sequential metal deposition can be used to produce core−shell structures as well as overlayers on high-surface-area catalysts. In this contribution, we describe the synthesis of fractional overlayers of Pt or Pd on Ru nanotube analogues of extended polycrystalline surfaces and apply these catalysts to the electrochemical hydrogen oxidation reaction (HOR) in alkaline electrolyte. The synthetic approach is shown schematically in Figure 1.

■ EXPERIMENTAL DETAILS

Nanotube Synthesis. Platinum−ruthenium and palladium−ruthenium nanotubes were synthesized by consecutive vapor depositions, first of platinum or palladium, and followed by ruthenium, in a modified chemical vapor deposition technique that has been detailed recently for the synthesis of Pt-rich, alloyed PtRuNTs.[49] For these Ru-rich PtRuNTs and PdRuNTs, the more noble of the metals in the nanotube samples was deposited first within the channels of a porous anodic alumina (AAO) membrane (Whatman Anodisc, 13 mm diameter, 200 nm pore size), seeding the template for the subsequent deposition of ruthenium in a separate vapor deposition. Each isolated precursor powder (Alfa Aesar) was contained under the template prior to a mild heat treatment under vacuum and ranging in temperature from 160 °C for palladium acetylacetonate to 210 °C for platinum acetylacetonate and 240 °C for ruthenium acetylacetonate. The masses of the metalorganic precursors applied were adjusted to control the amounts of the metals deposited for a range of Ru-rich compositions. Pure metal samples were also prepared by the lone addition of the metal to the alumina template in a single vapor deposition experiment. After 15 h at the appropriate temperature for precursor decomposition and metal deposition within the templates, the oven was evacuated and flushed with dry N_2 several times and cooled to room temperature. Finally, the mass of the deposited metal was measured to determine the nominal composition of the nanotube sample that was later confirmed by scanning electron microscopy coupled with energy-dispersive spectroscopy (SEM-EDS).

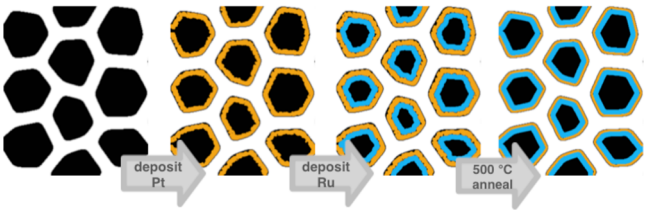

Figure 1. Synthesis scheme illustrating the sequence of precursor deposition used to make bimetallic nanotubes, depicting nanotube cross sections in the anodic alumina template. Following annealing, the nanotubes are separated from the template in 30% KOH then analyzed using microscopic, spectroscopic, and electrochemical techniques.

Ruthenium was deposited as a hydrous oxide along the Pt- or Pd-lined template walls,[49] and after vapor deposition of the materials, the templates were thermally annealed in a forming gas to induce morphological transitions, oxide reduction, and grain growth. The metal-lined templates were annealed in a quartz tube furnace with a flowing 4% H_2 environment at 500 °C for 1 h, using a programmed temperature ramp rate of 5 °C/min. To characterize the nanotubes for further study, the sacrificial alumina templates were dissolved in KOH, the released nanotubes were settled passively, and the supernatant solution was decanted and replaced with water until the suspension reached a neutral pH.

Spectroscopy/Microscopy. *Scanning Electron Microscopy.* Scanning electron microscopy (SEM) images were obtained with a Zeiss Model 1525 Field Emission SEM at an accelerating voltage of 3 kV, using an in-lens electron detector. SEM-EDS measurements of nanotube chemical compositions were conducted at an accelerating voltage of 20 kV.

Scanning Transmission Electron Microscopy. A Hitachi NB-5000 focused-ion-beam (FIB) instrument was used to prepare thin cross sections of the PtRuNTs and PdRuNTs in the AAO template for scanning transmission electron microscopy (S/TEM) imaging and energy-dispersive spectroscopy (EDS) mapping with a JEOL Model 2200FS system operating at 200 kV.

X-ray Diffraction. X-ray diffraction (XRD) patterns were recorded with a Bruker Phaser D2 diffractometer using Ni-filtered Cu Kα radiation (λ = 0.154184 nm, 30 kV, 10 mA, 0.014° step, 0.5 s/step) in the Bragg−Brentano geometry fitted with a 0.6 mm antiscatter slit in the incident beam and a 2.5° Soller slit in the diffracted beam. The position and width of diffraction peaks were obtained by fitting to Voigt functions, using IGOR Pro (Wavemetrics, Inc.).

X-ray Absorption Spectroscopy. X-ray absorption spectroscopy (XAS) was conducted at Beamline 20-BM at the Advanced Photon Source at Argonne National Laboratory (Argonne, IL, USA). Pre-edge correction, normalization, and postedge subtraction via spline fitting were done in Athena.[50]

DOI: 10.1021/acscatal.5b01432
ACS Catal. 2015, 5, 7015−7023

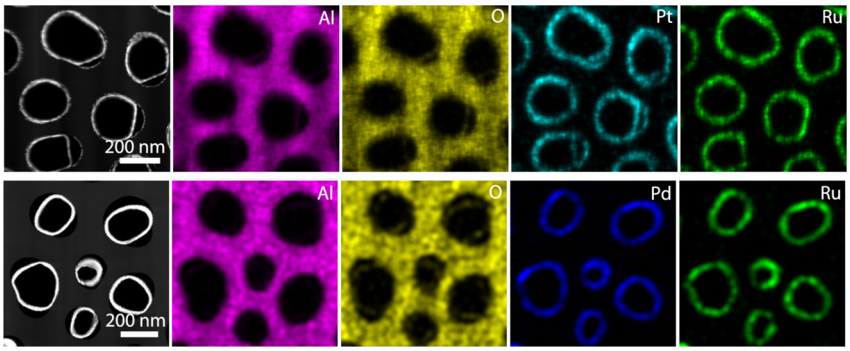

Figure 2. Scanning tunnelling electron microscopy (STEM) images from focused-ion-beam (FIB)-prepared cross sections of (top) PtRuNTs (19% Pt) and (bottom) PdRuNTs (22% Pd) within the anodic alumina template.

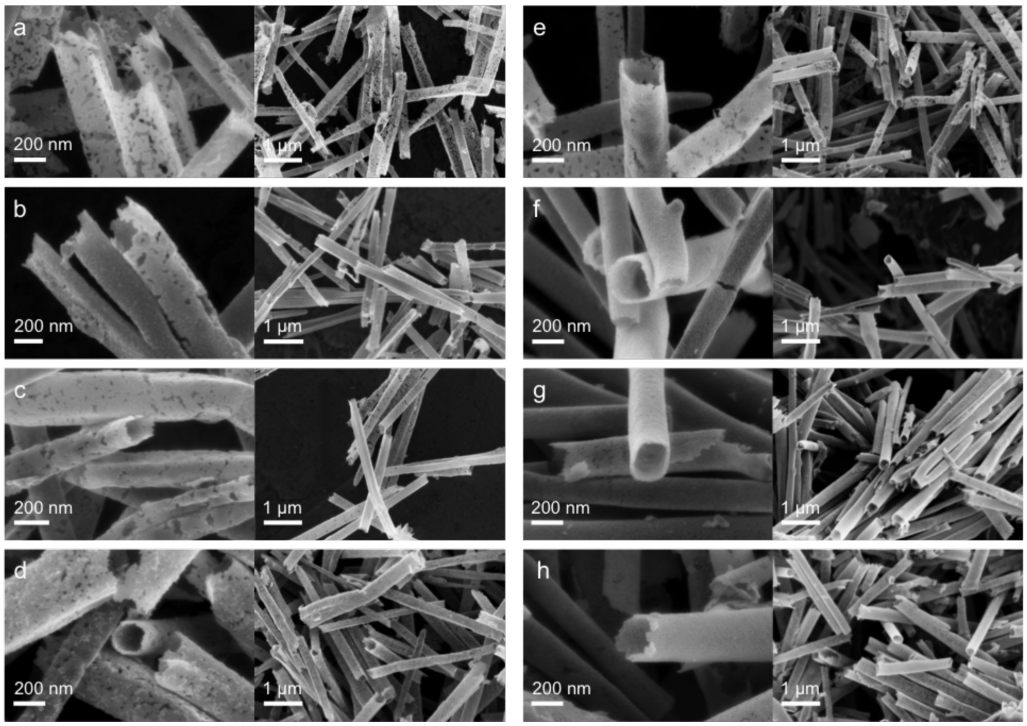

Figure 3. SEM images of PtRuNTs with (a) 4% Pt, (b) 7% Pt, (c) 10% Pt, and (d) 19% Pt, and PdRuNTs with (e) 7.5% Pd, (f) 18% Pd, (g) 19% Pd, and (h) 22% Pd after heat treatment.

The k^2-weighted $\chi(k)$ forward Fourier transform (FT) parameters were as follows: window, Hanning; k-range, 2−16 Å^{-1}. The k^2-weighted χ(R) backward FT parameters were as follows: window, Hanning; R-range, 1−3 Å. Atomic first-shell scattering paths were determined for tetrahedral geometry (face-center, close-packed systems) for the Pt, Pd, and Ru EXAFS data in Artemis and were used in FEFF[51,52] to determine scattering paths. Interference patterns were simulated simultaneously for all possible metal−metal scattering paths, and parameters were fit in Artemis.[53]

Electrochemical Characterization. Electrocatalysts were tested at room temperature in a standard three-electrode electrochemical cell (Pine Instruments) with a double-junction Ag/AgCl reference electrode (Pine Instruments) and Pt-wire counter electrode in H_2-saturated, 0.1 M potassium hydroxide (semiconductor grade, Sigma−Aldrich). Electrodes were made by depositing well-dispersed catalyst nanotubes onto glassy-carbon electrodes (wiith an area of A = 0.196 cm^2) for a target catalyst load of ∼7 μg Pt-group metal/cm^2. Polarization curves were obtained over the range −0.1−1.025 V vs RHE, using a Bio-Logic VMP3 research-grade multichannel potentiostat with EC-Lab software. Potentiostatic electrochemical impedance spectroscopy (EIS) spectra were recorded from 200 kHz to 1 Hz at 0.4 V vs RHE with a 10 mV sine perturbation amplitude under H_2 mass-transport-limited conditions and 1 atm H_2. The high-frequency intercept of the EIS spectrum was used to eliminate the ohmic resistance of the electrochemical cell from the polarization curves. Electrochemical active surface areas (ECSAs) were obtained using Cu-stripping techniques.[54]

■ RESULTS AND DISCUSSION

Vapor-phase deposition yields uniform, nanoscale, two-dimensional (2D) catalysts with high activity from as-received precursors that mimic extended polycrystalline surfaces, allowing for fine discrimination in the geometric and electronic characteristics important to various electrochemical reactions. Conformal coatings of Pt or Pd are first vapor-grown within the channels of a porous anodic alumina template. Following the

DOI: 10.1021/acscatal.5b01432
ACS Catal. 2015, 5, 7015−7023

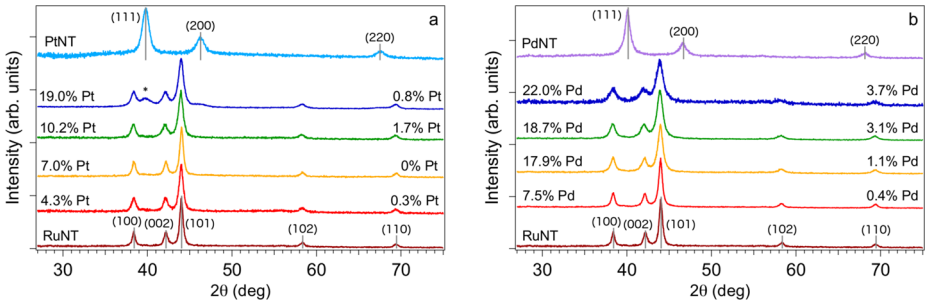

Figure 4. Cu Kα XRD patterns for the (a) PtRuNTs and (b) PdRuNTs with reference spectra for the monometallic RuNT, PtNT, and PdNT included. Above the respective spectra, the nominal composition is reported on the left, while the composition determined using Vegard's law is given on the right. Pure metal peak positions with relative intensities (gray sticks) are included for reference (Ru, Joint Committee for Powder Diffraction Standards (JCPDS) Powder Diffraction File (PDF) No. 00-006-0663; Pt, JCPDS PDF No. 00-004-0802; and Pd, JCPDS PDF No. 00-005-0681).

deposition of the more-noble outer layer, Ru is deposited in the channels (Figure 1). HAADF STEM and EDS map images for cross sections of the PtRuNTs and PdRuNTs embedded within the alumina template are shown in Figure 2, following heat treatment. The aluminum and oxygen EDS maps in Figure 2 identify the porous alumina template. The nanotubes take a shape conformal to the template walls while the metal pairs are in close proximity. The nanotube samples were harvested for further study of their microstructures and for electrochemical characterization by dissolving the sacrificial template in KOH.

The SEM images in Figure 3 illustrate the high aspect ratio of the nanotube catalysts with lengths ranging from 2 μm to 20 μm that are roughly 200 nm in diameter with wall thicknesses of 10−15 nm. These results are consistent with previous applications of this technique.[49] As-synthesized, the nanotubes are nanoparticulate aggregates of 3−5 nm particles of the discretely layered materials. Following a thermal treatment at 500 °C, considerable Ru grain growth results accompanied by dewetting of template, generating nanoscale porosity observed in the nanotube walls as the small crystallites coalesce and form larger crystalline grains with smoother surfaces. Additional SEM images of the monometallic (Pt, Ru, Pd) nanotube control samples may be found in Figure S1 in the Supporting Information.

The heat-treated nanotubes have nanosized grains with the hexagonal close packed (hcp) crystal structure of the Ru nanotube, as illustrated in Figure 4. EDS analysis was used to confirm the relative atomic composition of the nanotubes, while a simple Vegard's law approach[46] was used to investigate the degree of alloying. Above each diffraction pattern in Figure 4 is the respective sample's nominal composition (given on the left) and the composition calculated from the hcp (100) peak position using Vegard's law (given on the right), while the lattice reflections for the monometallic species are labeled.

As expected, based on the nominal composition, the hcp phase is the dominant crystal structure, but it lacks the lattice expansion that would be expected from a substitutional alloy of the nominal composition that would have been evidenced by shifts of the lattice reflections to smaller angles. The compositions calculated from shifts of the hcp (100) diffraction peak are suggestive of significant phase segregation in the nanotubes. Thermodynamic calculations and experimental evidence suggest that over 90% of the Pt is expected to phase segregate.[55] The tendency to segregate for the PdRuNTs is even stronger.[55−58] Here, thermodynamics and sequential chemical vapor deposition both favor the tendency to form segregated structures.

The results of a Scherrer analysis indicate no large differences between measured grain sizes for each of the Ru diffraction peaks, suggesting that the high aspect ratio of these vapor-grown nanotubes does not cause grain anisotropy. Grain size results for the different lattice directions are reported in Table S1 in the Supporting Information.

For high Pt fractions, the diffraction pattern for the 19% Pt sample also contains a distinct and broad (111) diffraction peak attributed to discrete Pt islands (indicated by an asterisk (*) in Figure 4). The broadness of the Pt(111) peak is suggestive of small grain sizes, relative to the much larger Ru grains.

Electronic interactions, probed using X-ray absorption near edge spectroscopy (XANES), reveal that the Ru phase behaves like Ru foil while Pt and Pd phases show increased valence band filling and lattice compression. For all of the bimetallic nanotube samples, regardless of composition, the Ru electronic structures are virtually indistinguishable from Ru foil and pure Ru nanotubes, as illustrated in Figure 5. Such behavior indicates that the Ru phase is predominately metallic without metal oxide or alloy formation. In the PtRuNTs, the Pt L_3-edge probes the majority of available electronic transitions in its bonding *d*-orbital and reductions in the observed white line intensity vs Pt foil are consistent with electron donation from Ru to Pt.[59,60] Analogous behavior in the PdRuNTs at the Pd K-edge cannot be observed because K-edge transitions do not probe electron promotion into *d*-orbital vacancies in Pd.

Some structural information can also be obtained from the near-edge data. The Pt and Pd white line peaks broaden in both sets of bimetallic nanotubes. In this case, the broadening is a subtle and significant distinction from a shift of the white line to lower energies. Here, peak broadening indicates lattice compression of the Pt or Pd from the underlying large Ru grains. Calculations have shown that metal *d*-bands expand and become less tightly bound as metal lattices are compressed.[58,61] Such behavior would lead to broadening of the Pt and Pd white line peaks without a shift of the white line peak energy.[58,61] As Pt or Pd composition increases, the white line peaks progressively broaden. This behavior is consistent with increased interatomic compressive forces in more-complete overlayers. Examples of changes in XANES for compressive or tensile strain have been presented in the literature; however, our data represent a more definitive example than is typically presented and represent a strength of this synthesis technique to investigate phase-segregated structures.[62−64]

DOI: 10.1021/acscatal.5b01432
ACS Catal. 2015, 5, 7015−7023

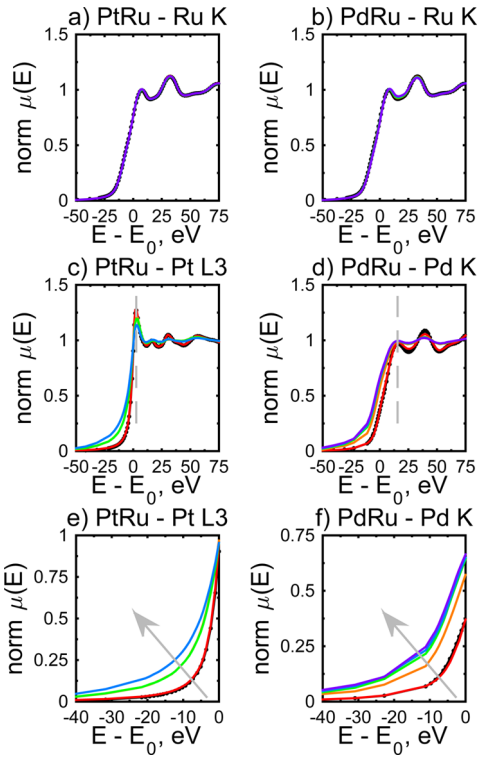

Figure 5. Normalized XANES spectra for (a, c, e) the PtRuNT nanotubes and (b, d, f) PdRuNT nanotubes at the Ru K-edge (panels a and b), Pt L_3-edge (panels c and e), and Pd K-edge (panels d and f). Gray guides (vertical dashed lines) in panels c and d are present to guide the eye to the center of the white line peak. The location of the white line peak remains fixed as the pre-edge moves, which is suggestive of white line peak broadening from compressive strain with increasing Pt (or Pd) content. Data for the reference foil (black dotted line) and their respective pure metal nanotubes (red) are included in each figure for comparison. Key: $Ru_{0.93}Pt_{0.07}$ (orange), $Ru_{0.87}Pt_{0.13}$ (green), $Ru_{0.69}Pt_{0.31}$ (blue); $Ru_{0.93}Pd_{0.07}$ (orange), $Ru_{0.85}Pd_{0.15}$ (green), $Ru_{0.80}Pd_{0.20}$ (blue), $Ru_{0.77}Pd_{0.23}$ (violet). Gray arrows indicate increasing Pt (panel e) or Pd (panel f) composition and increased peak broadening in the enlarged pre-edge XANES spectra for the Pt L_3- and Pd K-edges, respectively.

For both the Pt L_3 and Pd K XANES behavior, we conclude that electron density is transferred from the Ru to the Pt or Pd and that there is evidence of compressive strain in the Pt and Pd, which is suggestive of segregation of tightly bound Pd or Pt atop Ru nanotubes. We expect that electron donation from the Ru to the Pt or Pd would reduce the hydrogen-binding energy, leading to improved HOR activity. In addition, compressive strain should increase hybridization at the valence band from expanded *d*-orbitals that should lead to increased electron filling and reduced interaction energy with adsorbed hydrogen. In both cases of compressive strain and electron donation from Ru to the surface metal, increased activity would be observed for the bimetallic nanotubes versus their pure metal counterparts.

The XANES observations are corroborated with atomic spacing information obtained using the forward FTs of the EXAFS spectra, illustrated in Figure 6. Ru K-edge EXAFS for all of the Ru-containing tubes show only Ru−Ru bonding interactions with no shifts related to either alloying or lattice strain. Bond lengths and EXAFS parameter fits are given in the Supporting Information (see Table S2).

Pd K-edge EXAFS show a compressed Pd−Pd first-shell scattering path. Estimations of bond lengths for the Pd−Pd

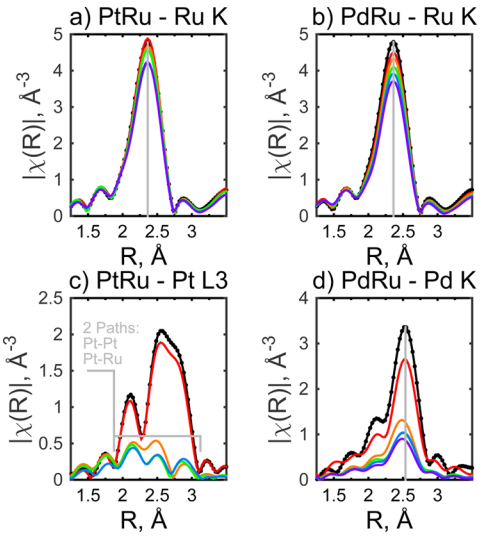

Figure 6. Forward Fourier transforms (FTs) of the EXAFS for (a, c) the PtRuNTs and (b, d) the PdRuNTs at the Ru K-edge (panels a and b), Pt L_3-edge (panel c), and Pd K-edges (panel d). Data for the reference foil (black dotted line) and their respective pure metal nanotubes (red) are included in each figure for comparison. The gray guides in panels a, b, and d are guides to the center of the first-shell scattering path. While the transform magnitude related to the two paths present in panel c are indicated by the gray guides. Key: $Ru_{0.93}Pt_{0.07}$ (orange), $Ru_{0.87}Pt_{0.13}$ (green), $Ru_{0.69}Pt_{0.31}$ (blue); $Ru_{0.93}Pd_{0.07}$ (orange), $Ru_{0.85}Pd_{0.15}$ (green), $Ru_{0.80}Pd_{0.20}$ (blue), $Ru_{0.77}Pd_{0.23}$ (violet).

scattering path from fitted spectra are ∼98.5% of the bond length in pure Pd foil (average of 2.702 Å vs 2.742 Å), which is indicative of substantial compressive strain in the Pd surface layer of the PdRuNTs. Such behavior, when considered with the Ru K-edge EXAFS, suggests complete phase segregation between Pd and Ru in the PdRuNTs. In addition, the reduction in the intensity of the Pd−Pd first-shell scattering path is consistent with lesser-coordinated, nanosized grains, as might be expected from a fractional overlayer.

In the PtRuNTs, there is evidence of Pt−Pt and Pt−Ru scattering paths. These data suggest complete phase segregation of the Pt from the Ru lattice with incorporation of small amounts of Ru into the Pt lattice, consistent with previous experimental data and thermodynamic calculations.[55] There are reductions in Pt−Pt bond length consistent with alloy formation or strain induced from the Ru nanotube support.[20] Estimations of bond lengths for the Pt−Pt scattering path in Pt L_3-edge first-shell fits are ∼99% of the bond length in pure Pt foil for each of the samples (average of 2.756 Å vs 2.764 Å). Because of the small reduction in bond length, the Ru−Pt scattering path is attributed to interfacial Ru−Pt mixing instead of alloy formation where more dramatic reductions in Pt−Pt bond lengths would be expected. For such structures, the ligand effects would be expected to propagate through the entirety of the Pt overlayer.[55] Examples of the EXAFS quality, as well as the Pt−Pt and Pt−Ru scattering path fitting, are illustrated in Figure S2.

We have demonstrated using XAS an ability to manipulate the electronic structure of the Pt and Pd overlayers via strain and ligand effects. The electrochemical data, illustrated in Figures 7a and 7b, show the influence of Ru on the charging behavior of Pt and Pd with composition-dependent shifts in three important potential regions (V vs RHE): (1) proton

DOI: 10.1021/acscatal.5b01432
ACS Catal. 2015, 5, 7015−7023

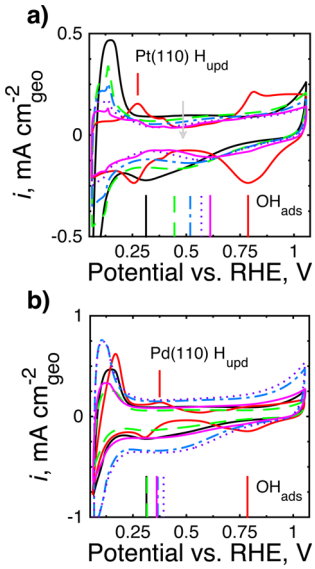

Figure 7. Electrochemical data collected in static, N_2-saturated, 0.1 M KOH at 50 mV/s for (a) the PtRuNTs and (b) the PdRuNTs. Charging currents indicate a composition-dependent reduction in the double-layer charging current for the PtRuNTs and a shift of the surface oxide reduction peak for both the PtRuNTs and the PdRuNTs. See text for a description of the gray arrow. Key: (a) RuNT (black), PtNT (red), $Pt_{0.04}Ru_{0.96}$NT (green), $Pt_{0.07}Ru_{0.93}$NT (blue), $Pt_{0.10}Ru_{0.90}$NT (purple), $Pt_{0.19}Ru_{0.81}$NT (magenta); (b) RuNT (black), PdNT (red), $Pd_{0.07}Ru_{0.93}$NT (green), $Pd_{0.15}Ru_{0.85}$NT (blue), $Pd_{0.20}Ru_{0.80}$NT (purple), $Pd_{0.23}Ru_{0.77}$NT (magenta).

adsorption/desorption (~0–0.3 V); (2) anodic double layer charging (~0.3–0.7 V); and (3) cathodic M–OH_{ads} reduction (~0.3–0.7 V).

In the proton adsorption/desorption region, the M–H binding energy is reduced on the surfaces of the nanotubes, with respect to monometallic Pt or Pd. This is evidenced by the shift of the broad H_{upd} region to lower potentials, in comparison to monometallic Pt or Pd. However, the characteristic polycrystalline (110) peak (ca. 0.25 V on Pt and 0.35 V on Pd) is not well-resolved for the bimetallic nanotubes and prevents rigorous quantitation in the change in M–H binding energy. This behavior is common for Pt and Pd alloys with Ru and represents a significant challenge in determining changes in M–H binding energy electrochemically. For now, we are left with only a general conclusion that the M–H binding energy is reduced. Later, we will show how changes in oxophilicity can be used as an effective probe for changes in surface electronics and, by analogy, M–H binding energy.

In the double-layer charging region (ca. 0.5 V vs RHE), the magnitude of the charge decreases as the Pt content increases (as indicated by the gray arrow in Figure 7a), suggesting increasingly complete Pt coverage. However, the double-layer charging region of the PdRuNTs is more difficult to interpret, because of larger variations in grain size (and, thus, double-layer charging).

The Ru–OH_{ads} reduction peak, ca. 0.331 V vs RHE on the monometallic RuNTs (in comparison to 0.79 V vs RHE on monometallic Pt or Pd), shifts systematically to higher potentials as indicated by the rightward shift of the bars with increasing adatom composition in Figures 7a and 7b. There is a large and systematic variation in the reduction potential of these surface oxides on the PtRuNTs (PtRuNTs: 0.44–0.61 V vs RHE). The variation for the PdRuNTs, while not as large, is also systematic with increasing Pd content (PdRuNTs: 0.31–0.40 V vs RHE).

Electron transfer from subsurface Ru to the Pt or Pd overlayers would increase the affinity of the Pt or Pd surface skins with adsorbed OH, making the reduction of surface oxides more difficult, versus their monometallic analogues, as is seen here. In charging currents such as those in Figure 7, surface oxides are generally of the form M–OH and are generated during anodic polarization of the electrode. During charging, as the potential is lowered from its maximum value (~1.1 V vs RHE), the surface oxides formed during anodic polarization are reduced, to restore the clean metal surface. The stronger the M–OH interaction, the lower the applied potential must be before the metal surface is restored. Ru is well-known to maintain a surface oxide at very low potentials[65] overlapping with the HOR potential region and can provide a source of adsorbed OH to complete the oxidation of adsorbed H, leading to the so-called "bifunctional effect". However, from these electrochemical data alone, it is not possible to indicate whether the OH is more closely associated with the Ru or Pt (Pd) surface sites. However, we can say with certainty that there is an increase in the surface oxophilicity and in the population of M–OH sites at applied potentials near 0 V vs RHE for the bimetallic tubes vs monometallic Pt or Pd.

From the collective structural and electrochemical data presented thus far, one would expect that hydrogen oxidation would be enhanced because of the ligand and strain effects for the Pt or Pd overlayers on the RuNTs. To highlight the impact of overlayer coverage on activity, the specific and intrinsic activities are summarized and discussed here, while the *iR*-corrected raw HOR data, as well as the processed/fitted kinetic currents are given in the Supporting Information (see Figures S3 and S4).

The specific activities of the bimetallic structures are all significantly increased vs their monometallic counterparts. The surface-area-normalized activities are given in Figure 8 and are considered with respect to the fractional overlayer coverage of Pt or Pd on Ru, which was calculated using a simple geometric

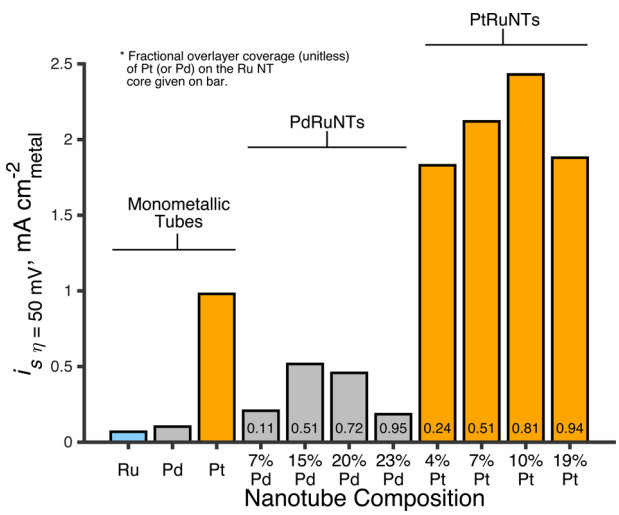

Figure 8. Specific activity of the various nanotube compositions. The Pt (or Pd) monolayer thickness is given on the bars for the bimetallic nanotubes. There are significant improvements in specific activity vs their constituent monometallic nanotubes, and the optimum performance is achieved at ~0.5–0.8 fractional overlayer coverage (unitless) for the PdRuNTs and PtRuNTs.

DOI: 10.1021/acscatal.5b01432
ACS Catal. 2015, 5, 7015–7023

model for the nanotubes and corroborated by their double-layer charging behavior. The value we calculate here is unitless and represents the nominal fraction of the Ru nanotube surface covered by either Pt or Pd on a scale of 0 to 1, where 1 denotes complete coverage. We find a strong variation in activity with overlayer coverage with a maximum at ∼0.5−0.8. By optimizing the structure of the nanotubes, we have synthesized the most active alkaline HOR catalyst reported to date with a specific activity of 2.4 mA/cm^2_{metal} at 50 mV vs RHE. This result is nearly 5 times greater than our recently reported activity on carbon-supported Pt nanoparticles (0.51 mA/cm^2_{Pt}) with dramatically increased Pt utilization efficiency: 1240 A/g_{Pt} for the optimized nanotube vs 280 A/g_{Pt} for carbon-supported Pt nanoparticles.[4] The similar factor of ∼2.5 increase for the PtRuNTs and PdRuNTs, with respect to their monometallic counterparts, suggests similar reductions in M−H binding energy (as described by a Brønsted−Evans−Polany relationship if the hydrogen binding energy is proportional to the difference in the activation energy[6]). Detailed results and fitted parameters are given in Table S3 in the Supporting Information.

Charging currents suggest a reduction in the hydrogen binding energy of the bimetallic tubes by a general shift of the H_{UPD} desorption features to more anodic potentials, but this is only qualitative. However, changes in the oxygen binding energy (oxophilicity) should describe the same electronic changes and thus correlate with changes in the hydrogen binding energy. Therefore, we use the ORR half-wave potential in an attempt to quantify changes in surface electronic effects. ORR is a well-studied phenomenon in electrocatalysis research and is an electrochemically accessible measure of surface electronic state that is known to correlate with *d*-band spacing in alkaline and acidic electrolytes.[16,66−72]

ORR data were collected for the monometallic and bimetallic nanotubes. The data were normalized to their mass-transport limited currents and their respective half-wave potentials were measured (see Figure S5 in the Supporting Information). We plot, in Figure 9, the HOR exchange current density (i_0), with respect to the ORR half-wave potential.

The collected results illustrate a volcano-like dependence of i_0 whose activity reaches a maximum at a half-wave potential of approximately −0.86 vs RHE. We have interpolated a *d*-band center scale using calculated results provided in the literature[70] and the ORR half-wave potentials of the monometallic Ru and Pt nanotubes. The maximum activity on this interpolated *d*-band center scale is ca. −2.1 eV, relative to the Fermi level. The corresponding interpolated values of the *d*-band centers for the bimetallic nanotubes correspond closely to the calculated values for fractional overlayers on Ru. For the PdRuNTs: −1.59 (calculated) vs −1.55 (experimental mean). For the PtRuNTs: −2.11 (calculated) vs −2.00 (experimental mean).

While the volcano correlation of the *d*-band center with exchange current density suggests a strong role for the electronic structure in determining HOR activity, there are additional meaningful conclusions that can be drawn from changes in Tafel slope, with respect to overlayer coverage. The Tafel slope describes how the current changes with respect to the applied potential and is characteristic of the interfacial reaction kinetics.[73] Consequently, it can be used to determine the rate-determining step (rds) by comparing it to the results from microkinetic models for a hypothesized HOR mechanism.[9] If more than one rds is present, the Tafel slope is an active-site-weighted average of the collected rds at different

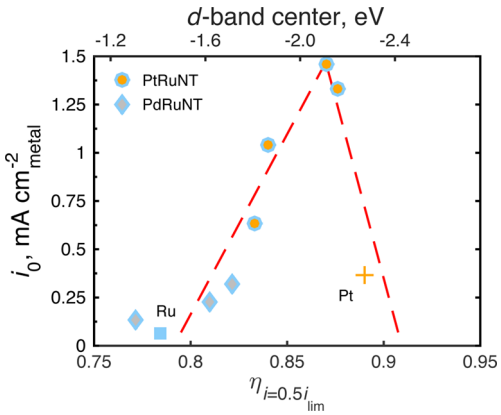

Figure 9. HOR exchange current density, with respect to the half-wave potential for ORR in O_2-saturated, 0.1 M KOH for the (■) RuNT, (♦) PdRuNTs, (●) PtRuNTs, and (+) PtNT. Dashed guides are present only the guide the eye. The *d*-band center scale was determined using calculated values for the monometallic RuNTs and PtNTs.[70] Interpolated *d*-band centers are similar to calculated values for fractional overlayers of Pt or Pd on Ru (see text). Pd samples that formed Pd−H during HOR (as determined by their ∼0.25 anodic transfer coefficient) exhibited an unusually low activity, because of hydride formation,[4] and have been omitted from the chart, for the sake of clarity.

active sites, i.e., it will lie intermediate to the respective Tafel slopes for the various rds.

On the PtRuNTs, the Tafel slope (86−94 mV/dec) is intermediate to the values expected for a purely hydrogen dissociative rds (∼30 mV/dec) and for a purely symmetric electron transfer rds (∼120 mV/dec). (See Table S3 in the Supporting Information for values.) The results here tell us that both ligand effects and bifunctional active sites are present on the PtRuNTs, as conceptualized in Figure 10.

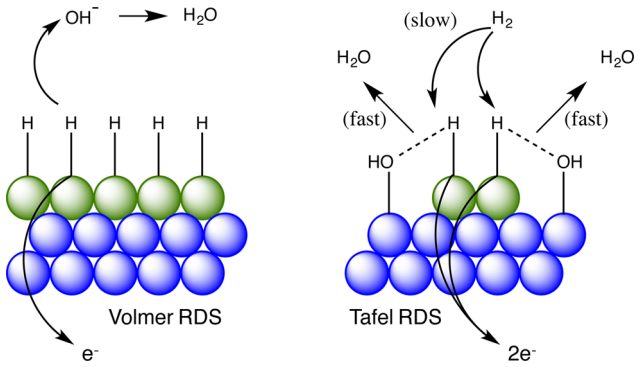

Figure 10. Schematic of Pt atoms (green) on Ru atoms (blue) comprising a PtRuNT showing active sites composed only of Pt atoms (left), as well as active sites of both Pt and Ru atoms (right). Electronic effects from the subsurface ligand reduce the hydrogen binding energy on both surfaces. On Pt atoms with adjacent OH, the electron transfer step is faster and the bifunctional active site clears the Pt atoms for slower H_2 dissociative adsorption (Tafel rate-determining step (rds)).

We hypothesize that ligand effects have reduced the M−H binding energy sufficiently on the PtRuNTs so that bifunctional effects are observable. This results in Tafel slopes intermediate between that of a hydrogen dissociative rds (30 mV/dec) and an electron transfer rds (120 mV/dec). This is in direct contrast to the PdRuNTs, where ligand effects have not reduced the M−H binding energy sufficiently to observe the bifunctional effect.

DOI: 10.1021/acscatal.5b01432
ACS Catal. 2015, 5, 7015−7023

Therefore, the observed Tafel slopes on the PdRuNTs are ~120 mV/dec, indicative of electron transfer as the sole rds on these structures. This behavior would be dependent on a similar intermediate species in both a hydrogen dissociative adsorption and electron transfer rds, namely, H_{ad}, as given in eqs 1, 2, and 3.

Tafel Reaction:

$$H_2 \leftrightarrows 2H_{ad} \quad (1)$$

Heyrovsky Reaction:

$$H_2 + OH^- \leftrightarrows H_{ad} + e^- + H_2O \quad (2)$$

Volmer Reaction:

$$H_{ad} + OH^- \leftrightarrows +e^- + H_2O \quad (3)$$

The data here exhibit no explicit differences in the H_{ad} described in the different HOR intermediate reactions. Instead, we see a smooth transition between PtRuNT structure, exchange current densities, and their corresponding Tafel slopes. Therefore, we interpret our results with respect to one type of adsorbed hydrogen intermediate whose interaction energy with the PtRuNTs has been sufficiently reduced to see both electron transfer and bifunctional effects during HOR. Such an interpretation is consistent with recent microkinetic modeling of the HOR/HER equilibrium where invoking different species of adsorbed hydrogen was not necessary to estimate the intrinsic activity of Pt.[74] In addition, the different microkinetic steps do not discriminate here between solution OH^- and surface-adsorbed OH_{ads}.

CONCLUSION

Ru nanotubes were used as analogues to extended polycrystalline surfaces to support Pt and Pd overlayers. The HOR activity of these bimetallic nanotubes varies with the nominal thickness of the Pt or Pd overlayer to yield electrocatalysts with optimal bifunctional, strain and ligand effects. Using ORR half-wave potential as an electrochemical proxy for *d*-band spacing, we find a maximum activity for calculated shifts around −2.1 eV versus the Fermi level. On optimally constructed tubes with fractional surface coverage of Pt on Ru nanotubes, we observe a mixed active-site population alternatively governed by hydrogen dissociative adsorption or electron transfer, yielding Tafel slopes intermediate between 30 and 120 mV/dec. Therefore, both theoretical rate-determining steps proposed in the literature may be observed in accord with the nanoscale proximity of active sites. The vapor-grown, bimetallic nanotubes used here have successfully translated the gains typically seen for epitaxially grown films on extended surfaces to realizable, nanoscale electrocatalysts.

ASSOCIATED CONTENT

Supporting Information

The Supporting Information is available free of charge on the ACS Publications website at DOI: 10.1021/acscatal.5b01432.

SEM images of the monometallic nanotubes used as controls (Figure S1); Scherrer analysis of all Ru hcp peaks of the XRD patterns for pure RuNT, PtRuNTs, and PdRuNTs annealed at 500 °C in 4% H_2 (Table S1); EXAFS fits (Table S2); k^2-weighted EXAFS at the Pt L3-edge for the Pt foil and the RuPt nanotubes (Figure S2); detailed description of the collected electrochemical data and its subsequent analysis (including discussion, equations, Figures S3−S6, and Table S3) (PDF)

AUTHOR INFORMATION

Corresponding Author

*Tel.: (865) 974-2421. Fax: (865) 974-7076. E-mail: apapandrew@utk.edu.

Notes

The authors declare no competing financial interest.

ACKNOWLEDGMENTS

This work was supported by the Office of Naval Research (No. N00014-12-1-0887) and the NSF-funded TN-SCORE program (No. EPS-1004083), under Thrust 2. Microscopy was conducted as part of a user proposal at the Center for Nanophase Materials Sciences (CNMS), which is sponsored at Oak Ridge National Laboratory by the Scientific User Facilities Division, Office of Basic Energy Sciences, U.S. Department of Energy. This research used resources of the Advanced Photon Source, a U.S. Department of Energy (DOE) Office of Science User Facility operated for the DOE Office of Science by Argonne National Laboratory (under Contract No. DE-AC02-06CH11357).

REFERENCES

(1) Varcoe, J. R.; Atanassov, P.; Dekel, D. R.; Herring, A. M.; Hickner, M. A.; Kohl, P. A.; Kucernak, A. R.; Mustain, W. E.; Nijmeijer, K.; Scott, K.; Xu, T.; Zhuang, L. *Energy Environ. Sci.* **2014**, *7* (10), 3135−3191.

(2) Varcoe, J. R.; Slade, R. C. T.; Lam How Yee, E. *Chem. Commun.* **2006**, No. 13, 1428−1429.

(3) Blizanac, B. B.; Ross, P. N.; Marković, N. M. *J. Phys. Chem. B* **2006**, *110* (10), 4735−4741.

(4) St. John, S.; Atkinson, R. W.; Unocic, R. R.; Zawodzinski, T. A., Jr.; Papandrew, A. B. *J. Phys. Chem. C* **2015**, *119* (24), 13481−13487.

(5) Strmcnik, D.; Uchimura, M.; Wang, C.; Subbaraman, R.; Danilovic, N.; van der Vliet, D.; Paulikas, A. P.; Stamenkovic, V. R.; Markovic, N. M. *Nat. Chem.* **2013**, *5* (4), 300−306.

(6) Durst, J.; Siebel, A.; Simon, C.; Hasche, F.; Herranz, J.; Gasteiger, H. A. *Energy Environ. Sci.* **2014**, *7* (7), 2255−2260.

(7) Koper, M. T. M. *Chem. Sci.* **2013**, *4* (7), 2710−2723.

(8) Sheng, W.; Zhuang, Z.; Gao, M.; Zheng, J.; Chen, J. G.; Yan, Y. *Nat. Commun.* **2015**, *6*, 5848.

(9) Krischer, K.; Savinova, E. R. In *Handbook of Heterogeneous Catalysis*; Wiley−VCH Verlag GmbH & Co. KGaA: Weinheim, Germany, 2008.

(10) Hori, Y.; Murata, A.; Kikuchi, K.; Suzuki, S. *J. Chem. Soc., Chem. Commun.* **1987**, No. 10, 728−729.

(11) Katsounaros, I.; Schneider, W. B.; Meier, J. C.; Benedikt, U.; Biedermann, P. U.; Cuesta, A.; Auer, A. A.; Mayrhofer, K. J. J. *Phys. Chem. Chem. Phys.* **2013**, *15*, 8058−8068.

(12) Schouten, K. J. P.; van der Niet, M. J. T. C.; Koper, M. T. M. *Phys. Chem. Chem. Phys.* **2010**, *12* (46), 15217−15224.

(13) Herrero, E.; Chen, Q.-S.; Hernández, J.; Sun, S.-G.; Feliu, J. M. *Phys. Chem. Chem. Phys.* **2011**, *13* (37), 16762−16771.

(14) Hatsukade, T.; Kuhl, K. P.; Cave, E. R.; Abram, D. N.; Jaramillo, T. F. *Phys. Chem. Chem. Phys.* **2014**, *16* (27), 13814−13819.

(15) Li, D.; Wang, C.; Strmcnik, D. S.; Tripkovic, D. V.; Sun, X.; Kang, Y.; Chi, M.; Snyder, J. D.; van der Vliet, D.; Tsai, Y.; Stamenkovic, V. R.; Sun, S.; Markovic, N. M. *Energy Environ. Sci.* **2014**, *7* (12), 4061−4069.

(16) Adzic, R. R.; Zhang, J.; Sasaki, K.; Vukmirovic, M.; Shao, M.; Wang, J.; Nilekar, A.; Mavrikakis, M.; Valerio, J.; Uribe, F. *Top. Catal.* **2007**, *46* (3), 249−262.

(17) Spendelow, J. S.; Lu, G. Q.; Kenis, P. J. A.; Wieckowski, A. *J. Electroanal. Chem.* **2004**, *568*, 215−224.

DOI: 10.1021/acscatal.5b01432
ACS Catal. 2015, 5, 7015−7023

(18) Spendelow, J. S.; Wieckowski, A. *Phys. Chem. Chem. Phys.* **2007**, *9* (21), 2654−2675.
(19) Watanabe, M.; Uchida, M.; Motoo, S. *J. Electroanal. Chem. Interfacial Electrochem.* **1987**, *229*, 395−406.
(20) Sasaki, K.; Mo, Y.; Wang, J. X.; Balasubramanian, M.; Uribe, F.; McBreen, J.; Adzic, R. R. *Electrochim. Acta* **2003**, *48* (25−26), 3841−3849.
(21) Zhang, J.; Vukmirovic, M. B.; Sasaki, K.; Nilekar, A. U.; Mavrikakis, M.; Adzic, R. R. *J. Am. Chem. Soc.* **2005**, *127* (36), 12480−12481.
(22) Zhang, J.; Mo, Y.; Vukmirovic, M. B.; Klie, R.; Sasaki, K.; Adzic, R. R. *J. Phys. Chem. B* **2004**, *108* (30), 10955−10964.
(23) Duan, Z.; Wang, G. *J. Phys. Chem. C* **2013**, *117* (12), 6284−6292.
(24) Greeley, J.; Jaramillo, T. F.; Bonde, J.; Chorkendorff, I.; Norskov, J. K. *Nat. Mater.* **2006**, *5* (11), 909−913.
(25) Yamada, Y.; Miyamoto, K.; Hayashi, T.; Iijima, Y.; Todoroki, N.; Wadayama, T. *Surf. Sci.* **2013**, *607*, 54−60.
(26) Wadayama, T.; Yoshida, H.; Ogawa, K.; Todoroki, N.; Yamada, Y.; Miyamoto, K.; Iijima, Y.; Sugawara, T.; Arihara, K.; Sugawara, S.; Shinohara, K. *J. Phys. Chem. C* **2011**, *115* (38), 18589−18596.
(27) Rettew, R.; Cheng, S.; Sauerbrey, M.; Manz, T.; Sholl, D.; Jaye, C.; Fischer, D.; Alamgir, F. *Top. Catal.* **2013**, *56* (12), 1065−1073.
(28) Rettew, R. E.; Allam, N. K.; Alamgir, F. M. *ACS Appl. Mater. Interfaces* **2011**, *3* (2), 147−151.
(29) Abdelhafiz, A.; Vitale, A.; Joiner, C.; Vogel, E.; Alamgir, F. M. *ACS Appl. Mater. Interfaces* **2015**, *7* (11), 6180−6188.
(30) Zhou, W. P.; Axnanda, S.; White, M. G.; Adzic, R. R.; Hrbek, J. *J. Phys. Chem. C* **2011**, *115* (33), 16467−16473.
(31) Zheng, Q. W.; Fan, C. J.; Zhen, C. H.; Zhou, Z. Y.; Sun, S. G. *Electrochim. Acta* **2008**, *53* (21), 6081−6088.
(32) Spendelow, J. S.; Babu, P. K.; Wieckowski, A. *Curr. Opin. Solid State Mater. Sci.* **2005**, *9* (1−2), 37−48.
(33) Inoue, H.; Brankovic, S. R.; Wang, J. X.; Adžić, R. R. *Electrochim. Acta* **2002**, *47* (22−23), 3777−3785.
(34) Yang, L.; Vukmirovic, M. B.; Su, D.; Sasaki, K.; Herron, J. A.; Mavrikakis, M.; Liao, S.; Adzic, R. R. *J. Phys. Chem. C* **2013**, *117* (4), 1748−1753.
(35) Hsieh, Y.-C.; Zhang, Y.; Su, D.; Volkov, V.; Si, R.; Wu, L.; Zhu, Y.; An, W.; Liu, P.; He, P.; Ye, S.; Adzic, R. R.; Wang, J. X. *Nat. Commun.* **2013**, *4*, 246610.1038/ncomms3466.
(36) Zhang, J.; Lima, F. H. B.; Shao, M. H.; Sasaki, K.; Wang, J. X.; Hanson, J.; Adzic, R. R. *J. Phys. Chem. B* **2005**, *109* (48), 22701−22704.
(37) Zheng, J.; Cullen, D. a.; Forest, R. V.; Wittkopf, J. a.; Zhuang, Z.; Sheng, W.; Chen, J. G.; Yan, Y. *ACS Catal.* **2015**, *5* (3), 1468−1474.
(38) Han, B.; Carlton, C. E.; Kongkanand, A.; Kukreja, R. S.; Theobald, B. R.; Gan, L.; O'Malley, R.; Strasser, P.; Wagner, F. T.; Shao-Horn, Y. *Energy Environ. Sci.* **2015**, *8* (1), 258−266.
(39) Lu, Q.; Hutchings, G. S.; Yu, W.; Zhou, Y.; Forest, R. V.; Tao, R.; Rosen, J.; Yonemoto, B. T.; Cao, Z.; Zheng, H.; Xiao, J. Q.; Jiao, F.; Chen, J. G. *Nat. Commun.* **2015**, *6*, 6567.
(40) St. John, S.; Boolchand, P.; Angelopoulos, A. P. *Langmuir* **2013**, *29*, 16150−16159.
(41) Chen, T.-Y.; Liu, Y.-T.; Nguyen, H. M.; Fan, L.-J.; Wu, C.-Y.; Mark Luo, T.-J.; Lee, C.-H.; Yang, Y.-W.; Wen, T.-C.; Lin, T.-L. *J. Mater. Chem. A* **2013**, *1* (18), 5660−5669.
(42) St. John, S.; Hu, N.; Schaefer, D. W.; Angelopoulos, A. P. *J. Phys. Chem. C* **2013**, *117* (15), 7924−7933.
(43) St. John, S.; Nan, Z.; Hu, N.; Schaefer, D. W.; Angelopoulos, A. P. *J. Mater. Chem. A* **2013**, *1* (31), 8903−8916.
(44) Papandrew, A. B.; Chisholm, C. R. I.; Elgammal, R. A.; Özer, M. M.; Zecevic, S. K. *Chem. Mater.* **2011**, *23* (7), 1659−1667.
(45) Papandrew, A. B.; Atkinson, R. W., III; Unocic, R. R.; Zawodzinski, T. a. *J. Mater. Chem. A* **2015**, *3* (7), 3984−3987.
(46) Papandrew, A. B.; Chisholm, C. R. I.; Zecevic, S. K.; Veith, G. M.; Zawodzinski, T. A. *J. Electrochem. Soc.* **2013**, *160* (2), F175−F182.
(47) Atkinson, R. W.; Papandrew, A. B.; Zawodzinski, T. A. *Meet. Abstr.* **2013**, *MA2013−02* (15), 1246.
(48) Papandrew, A. B.; Atkinson, R. W.; Goenaga, G. A.; Kocha, S. S.; Zack, J. W.; Pivovar, B. S.; Zawodzinski, T. A. *J. Electrochem. Soc.* **2013**, *160* (8), F848−F852.
(49) Atkinson, R. W.; Unocic, R. R.; Unocic, K. A.; Veith, G. M.; Zawodzinski, T. A.; Papandrew, A. B. *ACS Appl. Mater. Interfaces* **2015**, *7* (19), 10115−10124.
(50) Ravel, B. *EXAFS Analysis with FEFF and FEFFIT*, Vol. 2; University of Washington: Seattle, WA, 2001.
(51) Rehr, J. J.; Kas, J. J.; Vila, F. D.; Prange, M. P.; Jorissen, K. *Phys. Chem. Chem. Phys.* **2010**, *12* (21), 5503−5513.
(52) Vila, F. D.; Rehr, J. J.; Kelly, S. D.; Bare, S. R. *J. Phys. Chem. C* **2013**, *117* (24), 12446−12457.
(53) Ravel, B. *Crystallography for the X-ray Absorption Spectroscopist*; University of Chicago: Chicago, IL, 2002.
(54) Shao, M.; Odell, J. H.; Choi, S.; Xia, Y. *Electrochem. Commun.* **2013**, *31*, 46−48.
(55) Gasteiger, H. A.; Ross, P. N., Jr.; Cairns, E. J. *Surf. Sci.* **1993**, *293* (1−2), 67−80.
(56) Strohl, J. K.; King, T. S. *J. Catal.* **1989**, *118* (1), 53−67.
(57) Tyson, W. R.; Miller, W. A. *Surf. Sci.* **1977**, *62* (1), 267−276.
(58) Gelatt, C. D.; Ehrenreich, H.; Weiss, J. A. *Phys. Rev. B: Condens. Matter Mater. Phys.* **1978**, *17* (4), 1940−1957.
(59) Mansour, A. N.; Cook, J. W., Jr.; Sayers, D. E. *J. Phys. Chem.* **1984**, *88* (11), 2330−2334.
(60) Mansour, A. N.; Cook, J. W.; Sayers, D. E.; Emrich, R. J.; Katzer, J. R. *J. Catal.* **1984**, *89* (2), 462−469.
(61) Davis, R. J.; Landry, S. M.; Horsley, J. A.; Boudart, M. *Phys. Rev. B: Condens. Matter Mater. Phys.* **1989**, *39* (15), 10580−10583.
(62) Shao, M. H.; Huang, T.; Liu, P.; Zhang, J.; Sasaki, K.; Vukmirovic, M. B.; Adzic, R. R. *Langmuir* **2006**, *22* (25), 10409−10415.
(63) Frenkel, A. I.; Small, M. W.; Smith, J. G.; Nuzzo, R. G.; Kvashnina, K. O.; Tromp, M. *J. Phys. Chem. C* **2013**, *117* (44), 23286−23294.
(64) Wanjala, B. N.; Loukrakpam, R.; Luo, J.; Njoki, P. N.; Mott, D.; Zhong, C.-J.; Shao, M.; Protsailo, L.; Kawamura, T. *J. Phys. Chem. C* **2010**, *114* (41), 17580−17590.
(65) Scott, F. J.; Mukerjee, S.; Ramaker, D. E. *J. Phys. Chem. C* **2010**, *114* (1), 442−453.
(66) Shao, M.; Liu, P.; Zhang, J.; Adzic, R. *J. Phys. Chem. B* **2007**, *111* (24), 6772−6775.
(67) Jiang, L.; Hsu, A.; Chu, D.; Chen, R. *J. Electrochem. Soc.* **2009**, *156* (3), B370−B376.
(68) Stamenkovic, V.; Mun, B. S.; Mayrhofer, K. J.; Ross, P. N.; Markovic, N. M.; Rossmeisl, J.; Greeley, J.; Norskov, J. K. *Angew. Chem., Int. Ed.* **2006**, *45* (18), 2897.
(69) Lima, F. H. B.; Zhang, J.; Shao, M. H.; Sasaki, K.; Vukmirovic, M. B.; Ticianelli, E. A.; Adzic, R. R. *J. Phys. Chem. C* **2007**, *111* (1), 404−410.
(70) Ruban, A.; Hammer, B.; Stoltze, P.; Skriver, H. L.; Nørskov, J. K. *J. Mol. Catal. A: Chem.* **1997**, *115* (3), 421−429.
(71) Hammer, B.; Nørskov, J. K. *Surf. Sci.* **1995**, *343* (3), 211−220.
(72) Norskov, J. K.; Rossmeisl, J.; Logadottir, A.; Lindqvist, L.; Kitchin, J. R.; Bligaard, T.; Jonsson, H. *J. Phys. Chem. B* **2004**, *108* (46), 17886−17892.
(73) Bard, A. J.; Faulkner, L. R. *Electrochemical Methods: Fundamentals and Applications*; Wiley: New York, 2006.
(74) Skúlason, E.; Tripkovic, V.; Björketun, M. E.; Gudmundsdóttir, S.; Karlberg, G.; Rossmeisl, J.; Bligaard, T.; Jónsson, H.; Nørskov, J. K. *J. Phys. Chem. C* **2010**, *114* (42), 18182−18197.

DOI: 10.1021/acscatal.5b01432
ACS Catal. 2015, 5, 7015−7023